The Astrophysical Journal, 593:599–610, 2003 August 20

COSMOLOGICAL SHOCK WAVES AND THEIR ROLE IN THE LARGE-SCALE STRUCTURE OF THE UNIVERSE

Dongsu Ryu,[1,2] Hyesung Kang,[2,3] Eric Hallman,[2] and T. W. Jones[2]
Received 2003 February 12; accepted 2003 May 7

ABSTRACT

We study the properties of cosmological shock waves identified in high-resolution, *N*-body/hydrodynamic simulations of a ΛCDM universe and their role on thermalization of gas and acceleration of nonthermal, cosmic-ray (CR) particles. External shocks form around sheets, filaments, and knots of mass distribution when the gas in void regions accretes onto them. Within those nonlinear structures, internal shocks are produced by infall of previously shocked gas to filaments and knots and during subclump mergers, as well as by chaotic flow motions. Due to the low temperature of the accreting gas, the Mach number of external shocks is high, extending up to $M \sim 100$ or higher. In contrast, internal shocks have mostly low Mach numbers. For all shocks of $M \geq 1.5$, the mean distance between shock surfaces over the entire computed volume is $\sim 4\ h^{-1}$ Mpc at present, or $\sim 1\ h^{-1}$ Mpc for internal shocks within nonlinear structures. Identified external shocks are more extensive, with their surface area ~ 2 times larger than that of identified internal shocks at present. However, especially because of higher preshock densities but also due to higher shock speeds, internal shocks dissipate more energy. Hence, the internal shocks are mainly responsible for gas thermalization as well as CR acceleration. In fact, internal shocks with $2 \lesssim M \lesssim 4$ contribute about one-half of the total dissipation. Using a nonlinear diffusive shock acceleration model for CR protons, we estimate the ratio of CR energy to gas thermal energy dissipated at cosmological shock waves to be about one-half through the history of the universe. Our result supports scenarios in which the intracluster medium contains energetically significant populations of CRs.

Subject headings: large-scale structure of universe — methods: numerical — shock waves

1. INTRODUCTION

According to cosmological *N*-body/hydrodynamic simulations, intergalactic shock waves develop as a consequence of the large-scale structure formation of the universe. Infall of baryonic gas toward sheets, filaments, and knots, as well as supersonic flows associated with hierarchical clustering, induce shocks (Quilis, Ibanez, & Saez 1998; Miniati et al. 2000; Miniati 2002; Gabici & Blasi 2003). Those cosmological shock waves, like most astrophysical shocks, are collisionless features mediated by collective, electromagnetic viscosities. Such viscosities rely on irregular magnetic field components, i.e., MHD wave turbulence that is self-excited by the streaming suprathermal particles produced during shock formation (Wentzel 1974; Kennel, Edmiston, & Hada 1985; Quest 1988).

The existence and character of these shocks is important for several reasons. Through dissipation the cosmological shock waves convert part of the gravitational energy associated with structure formation into heat and, thus, govern the gas thermal history in the universe. Thermal energy is then radiated away, manifesting the large-scale structure as well as the dynamics that created it (Cen & Ostriker 1999; Davé et al. 2001). At the same time, due to incomplete plasma thermalization at collisionless shocks, a sizeable portion of the shock energy can be converted into cosmic-ray (CR) energy (mostly ionic) via diffusive shock acceleration (DSA; for reviews, see Blandford & Eichler 1987; Malkov & Drury 2001). This nonthermal population represents a small fraction of the ion flux through a collisionless shock that leaks back upstream to become subject to DSA; that is, to be injected into the nonthermal population. Numerous nonlinear studies of DSA have shown that substantial fractions of the energy flux through strong shocks can be captured by the nonthermal populations (Berezhko, Ksenofontov, & Yelshin 1995; Ellison, Baring, & Jones 1996; Malkov 1999; Kang, Jones, & Gieseler 2002). Extensive nonlinear simulations by some of us incorporating a plasma-physics–based thermal leakage injection model into combined gas dynamic/CR diffusion-convection simulations found that strong shocks transfer up to about one-half of the initial shock kinetic energy to CRs by this process (Kang et al. 2002; Kang & Jones 2002).

There is clear evidence that one or more processes energize significant nonthermal particle populations in and around cosmic structures. A number of clusters have been found with diffuse synchrotron radio halos and/or radio relic sources, indicating the existence of relativistic electron populations in intracluster medium (ICM; Giovannini & Feretti 2000; Feretti 2003). In addition, some clusters have been reported to possess excess EUV and/or hard X-ray radiation compared to that expected from the hot, thermal X-ray–emitting ICM, most likely produced by inverse Compton scattering of cosmic microwave background radiation (CMBR) photons by CR electrons (Lieu et al. 1996; Fusco-Femiano et al. 1999). Also, it has been suggested that a fraction of the diffuse γ-ray background radiation could originate from the same process (Loeb & Waxmann 2000; Miniati 2002; Scharf & Mukherjee 2002). If some of those CR electrons have been energized at cosmological shock waves, the same process should have produced greater CR

[1] Department of Astronomy and Space Science, Chungnam National University, Daejeon 305-764, Korea; ryu@canopus.chungnam.ac.kr.
[2] Department of Astronomy, University of Minnesota, Minneapolis, MN 55455; hallman@msi.umn.edu, twj@msi.umn.edu.
[3] Department of Earth Sciences, Pusan National University, Pusan 609-735, Korea; kang@uju.es.pusan.ac.kr.

proton populations. Hence, although CR protons in the ICM have yet to be confirmed by the observation of γ-ray photons produced by inelastic collisions between CR and thermal-gas protons (Miniati et al. 2001b; Reimer et al. 2003), there may very well exist CR proton populations there whose pressure is comparable to the gas thermal pressure (Ensslin et al. 1997; Colafrancesco & Blasi 1998; Lieu et al. 1999).

The properties of cosmological shock waves in the large-scale structure of the universe were analyzed quantitatively by Miniati et al. (2000) using numerical simulations with 270^3 grid zones in a cubic comoving region of size 85 h^{-1} Mpc for a SCDM model and a ΛCDM model. They identified accretion shocks, merger shocks, and internal flow shocks that were formed by infall and hierarchical clustering and showed that the topology of these shocks is very complex. They found merger and internal flow shocks distributed over Mach numbers from 3 to 10 with a peak at $M \sim 5$ and accretion shock Mach numbers ranging between 10 and a few $\times 10^3$. In a recent study based on a higher resolution simulation with 512^3 grid zones in a cubic comoving region of size 50 h^{-1} Mpc for a ΛCDM model, Miniati (2002) showed that most dissipation involves shocks of modest strength, with $4 \lesssim M \lesssim 10$ accounting for $\sim$45% of total shock heating. On the other hand, through a semianalytic study, Gabici & Blasi (2003) found a Mach number distribution of merger-related shocks during large-scale structure formation with a peak at a much lower Mach number ($M \lesssim 1.5$).

In this paper, we critically reexamine the properties of cosmological shock waves with a new set of cosmic structure formation simulations. We quantify the characteristics of cosmological shock waves and estimate the dissipation, gas thermalization, and CR acceleration at those shocks. The capture of shocks in hydrodynamic simulations and the identification of shocks in such simulation data are affected by numerical details including resolution. Therefore, to validate our findings, we estimate the errors in our measured quantities through consistency checks and resolution convergence tests. This study adds valuable insights into the thermal history and nature of gas in the universe as well as nonthermal activities in the ICM. In § 2, simulations are detailed along with shock identification. The main results of shock characteristics and shock dissipation are described in § 3 and § 4, respectively, followed by a summary in § 5.

2. NUMERICS

2.1. *Simulations*

The cold dark matter cosmology with a cosmological constant (ΛCDM) was employed with the following parameters: $\Omega_{\rm BM} = 0.043$, $\Omega_{\rm DM} = 0.227$, and $\Omega_\Lambda = 0.73$, $h \equiv H_0/(100$ km s^{-1} Mpc$) = 0.7$, and $\sigma_8 = 0.8$. The above values are consistent with those fitted with the recent WMAP data (Bennett et al. 2003). A cubic region of comoving size 100 h^{-1} Mpc was simulated inside a computational box with 1024^3, 512^3, 256^3, 128^3, and 64^3 grid zones for gas and gravity and 512^3, 256^3, 128^3, 64^3, and 32^3 particles for dark matter. It allows a uniform spatial resolution of $\Delta l = 97.7\ h^{-1}$ kpc $- 1.57\ h^{-1}$ Mpc. The simulations were performed using a PM/Eulerian hydrodynamic cosmology code. The code is described in Ryu et al. (1993). But the version of the code used includes several updates. For instance, it now adopts the MC (monotonized central difference) limiter instead of the original minmod limiter. The update to the MC limiter was intended to enhance the density resolution and to capture shocks more sharply (see LeVeque 1997 for details).

We did not include in our simulations several physical processes, such as radiative cooling, galaxy/star formation, and feedback from galaxies and stars, that can play significant roles in determining conditions within cluster cores, nor reionization of the intergalactic medium that effectively sets a temperature floor to the intergalactic medium (IGM). Our primary goal is to study cosmological shocks that are mostly outside cluster core regions. We established a temperature floor as a part of our analysis procedure. The conclusions drawn in this study, hence, should not be significantly weakened by the exclusion of those additional physical processes.

2.2. *Shock Identification*

While shocks are automatically detected during the simulations by the Riemann solver within the hydrodynamics routine, there are additional steps necessary to identify and characterize shocks for analysis. We have done this as a postprocessing step using the simulation data at selected epochs. Ideally, explicitly three-dimensional flow motions should be considered in identifying shocks in simulation data. However, to simplify the analysis, we used a one-dimensional procedure applied successively in all three primary directions. A zone was tagged as a shock zone currently experiencing shock dissipation whenever these three criteria are met: (1) $\Delta T \times \Delta s > 0$, i.e., the gradients of gas temperature and entropy have the same sign; (2) $\nabla \times \boldsymbol{v} < 0$, i.e., the local flow is converging (where $\nabla \times \boldsymbol{v}$ is the divergence of three-dimensional velocity field); (3) $|\Delta \log T| \geq 0.11$, where in each case, we define central differences according to the scheme $\Delta Q = Q_{i+1} - Q_{i-1}$. The third condition corresponds to the temperature jump of a Mach 1.3 shock. Typically, a shock is represented by a jump spread over 2–3 tagged zones. Hence, we identified a shock center within the numerical shock where $\nabla \times \boldsymbol{v}$ is minimum and labeled this center as part of a shock surface.

The Mach number of shock centers, M, was calculated from the temperature jump across shocks, which is given by

$$\frac{T_2}{T_1} = \frac{(5M^2 - 1)(M^2 + 3)}{16M^2}\ , \qquad (1)$$

where T_2 and T_1 are the postshock and preshock temperatures. Shock centers identified in multiple directional passes were labeled by the maximum M. We followed only those portions of shock surfaces with $M \geq 1.5$ to avoid confusion from complex flow patterns and shock surface topologies associated with very weak shocks. In the actual simulations, the minimum gas temperature was set as the temperature of CMBR, that is, $T_{\rm min} = 2.7(1 + z)$, since photoionization and heating as well as radiative cooling were ignored. However, considering that significant reionization would have taken place by $z \sim 15$ (Haiman & Holder 2003), in post-processing we set the minimum gas temperature at $T_{\rm min} = 10^4$ K. The shock properties described below include that consistency adjustment.

Figure 1 shows a two-dimensional slice from the 1024^3 simulation isolating a typical group with X-ray emission-weighted temperature $T_{\rm X} \approx 1.3$ keV and X-ray luminosity $L_{\rm X} \approx 4.2 \times 10^{43}\ h$ ergs s^{-1}. The figure shows the locations

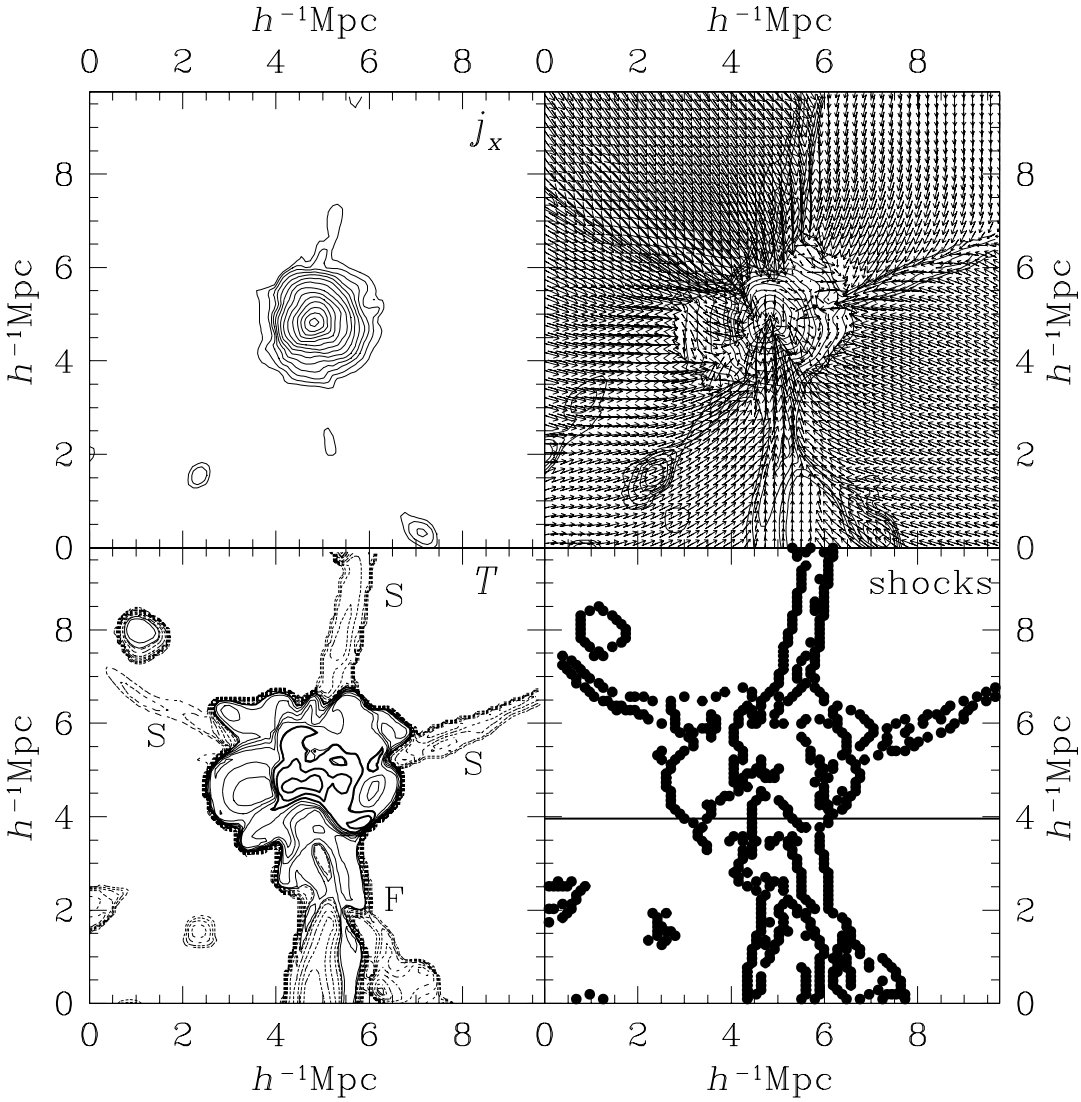

FIG. 1.—X-ray emissivity contours (*upper left panel*), velocity field superposed on density contours (*upper right*), gas temperature contours (*lower left*) and shock locations (*lower right*) in a two-dimensional slice of $(9.76\ h^{-1}\ \mathrm{Mpc})^2$ around a group of X-ray emission-weighted temperature $T_X \approx 1.3$ keV at $z = 0$. Contours of gas density $\rho_{\mathrm{gas}}/\langle\rho_{\mathrm{gas}}\rangle \geq 1$ are shown. Temperature contours are noted as follows: *Heavy solid lines*: $\log T > 6.8$; *Light solid lines*: $5.5 < \log T < 6.8$; *Dotted lines*: $4 < \log T < 5.5$. Several sheets and a filament were identified in the temperature contours.

of identified shocks along with the X-ray emissivity, gas temperature, density, and velocity field distributions. Although the X-ray emissivity distribution looks relatively smooth and round, there are complex accreting flows around the group including three sheets (*dotted line contours in the temperature contour map*) and one filament (*thin solid line contours*). A complex topology of shock surfaces surrounding the group can be seen in the temperature contour map and through the locations of identified shocks. The group as well as the associated sheets and filament are bounded by shocks, but there are several additional shock structures within that represent a variety of converging flow patterns. To illustrate the limitations of conventional spherical accretion concepts, we note that this group provides an example of structures where shocks can form in the core by organized infall flows accreting from filaments and sheets that penetrate deep into the center of potential wells. The Mach number of the surface along the portion of the accretion shock centered at $(x,\ y) = (3.5,\ 4.0)\ h^{-1}$ Mpc ranges over 2.4–4 with a mean value of 3.2, while that along the portion centered at $(x,\ y) = (5.5,\ 4.0)\ h^{-1}$ Mpc ranges 5.3–8.3 with a mean value of 6.5. Although quite strong shocks of Mach number of a few, including these, were often found within 0.5–1 h^{-1} Mpc from the center of clusters and groups, most shocks identified in our simulations are located outside the cores of clusters and groups (see the next section and Fig. 5).

In order to illustrate how our shock identification scheme works, we plot in Figure 2 the flow structure along the horizontal path drawn just below $y = 4\ h^{-1}$ Mpc in the shock location plot of Figure 1. As indicated in the upper right panel of the figure, two outer shocks with high Mach numbers and three inner shocks with lower Mach numbers were identified along the path. The existence of these five shocks is also clearly evident in the velocity field and temperature contours in Figure 1. Extensive tests showed that our scheme identifies shock surfaces reliably with a typical error of a few percent in Mach number.

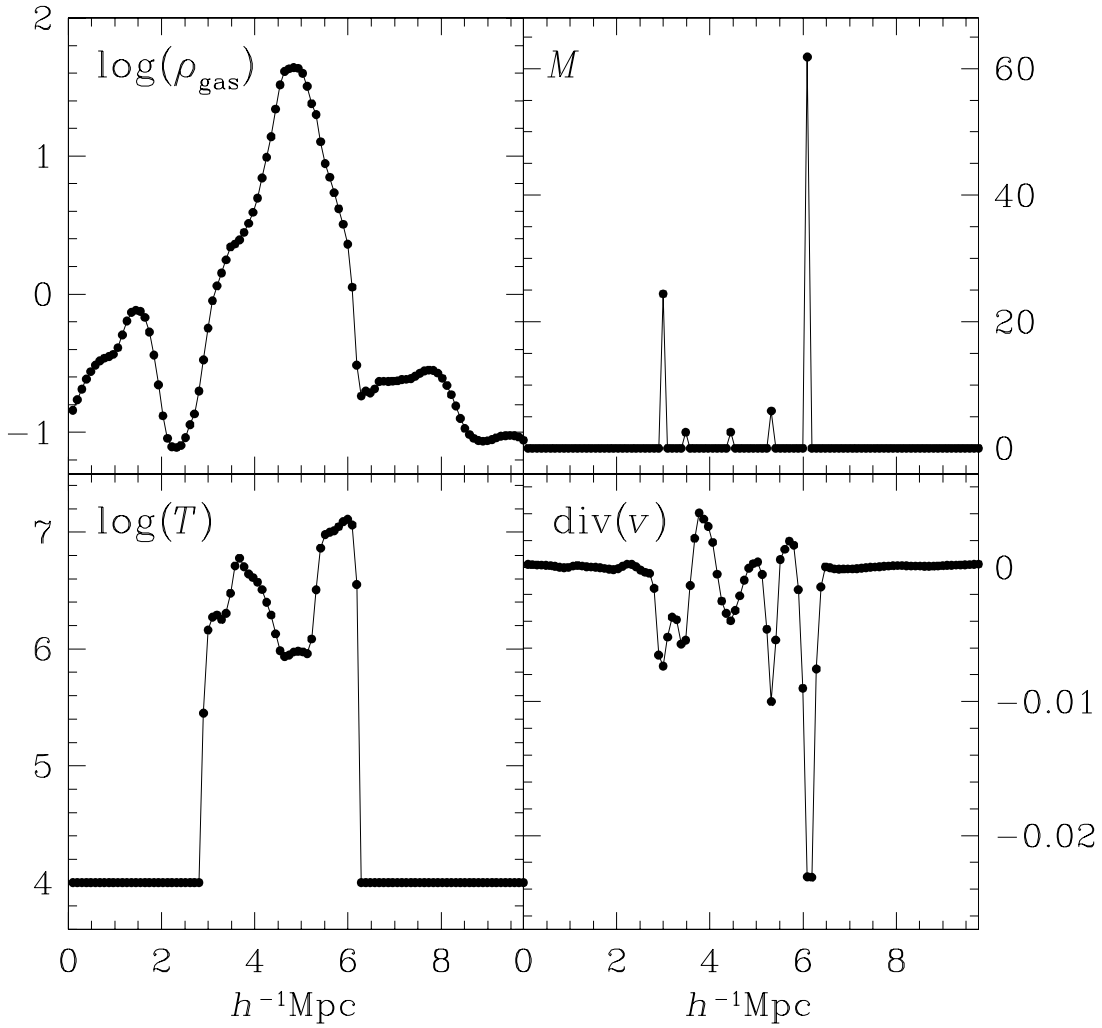

FIG. 2.—Flow structure along the line path drawn in Fig. 1, showing gas density, Mach number of identified shocks, gas temperature, and $\nabla \times \boldsymbol{v}$

3. PROPERTIES OF COSMOLOGICAL SHOCK WAVES

In previous studies by Miniati et al. (2000) and by other authors, cosmological shock waves were often organized into three categories; i.e., accretion shocks, merger shocks, and internal flow shocks. However, on the basis of close examination of shock locations and the properties of the shocks and their associated flows in our simulations, we suggest instead that it is very informative to classify cosmological shocks into two broad populations that can be conveniently labeled as *external* and *internal* shocks, depending on whether or not the associated preshock gas was previously shocked (that is, whether $T_1 \leq 10^4$ or greater than 10^4 for the preshock temperature in practice). This binary classification facilitates the understanding of their role in energy dissipation (see the next section). *External shocks* surround sheets, filaments, and knots, forming when never-shocked, low-density, void gas accretes onto those nonlinear structures. Subsequent *internal shocks* are distributed within the regions bounded by external shocks. They are produced by flow motions accompanying hierarchical structure formation inside the bounding shocks. For more refined questions, internal shocks can be further divided into three types: (1) accretion shocks produced by infall from sheets to filaments and knots and from filaments to knots, (2) merger shocks formed during subclump mergers, and (3) flow shocks induced by chaotic supersonic motions inside the nonlinear structures.

Figure 3 represents a two-dimensional slice of a $(25\ h^{-1}\ \mathrm{Mpc})^3$ volume extracted from the 1024^3 grid zone simulation. It shows the distributions of external and internal shocks in a cluster with X-ray emission-weighted temperature, $T_X \approx 3.3$ keV, and X-ray luminosity, $L_X \approx 1.4 \times 10^{45}\ h$ ergs s^{-1}, along with the gas density distribution and the velocity field of the inner parts of the slice. External shocks here define an entire cluster complex that has dimensions of about $(10 \times 10 \times 20)(h^{-1}\ \mathrm{Mpc})^3$. Numerous internal shocks were identified inside the complex. The two-dimensional velocity field demonstrates that infalls from several associated filaments and sheets form accretion shocks and also induce chaotic flow motions in the medium around the cluster. Figure 4 shows a three-dimensional view of shock surfaces around the same cluster complex. Surfaces of external shocks with high Mach numbers, represented with yellow, encompass the complex and filaments associated with it. Several sheets with lower Mach numbers, which intersect at the complex, are also clearly visible. These figures show clearly that the canonical spherical external accretion shock model around a cluster would be far too simple to apply to this sample cluster. Note, in

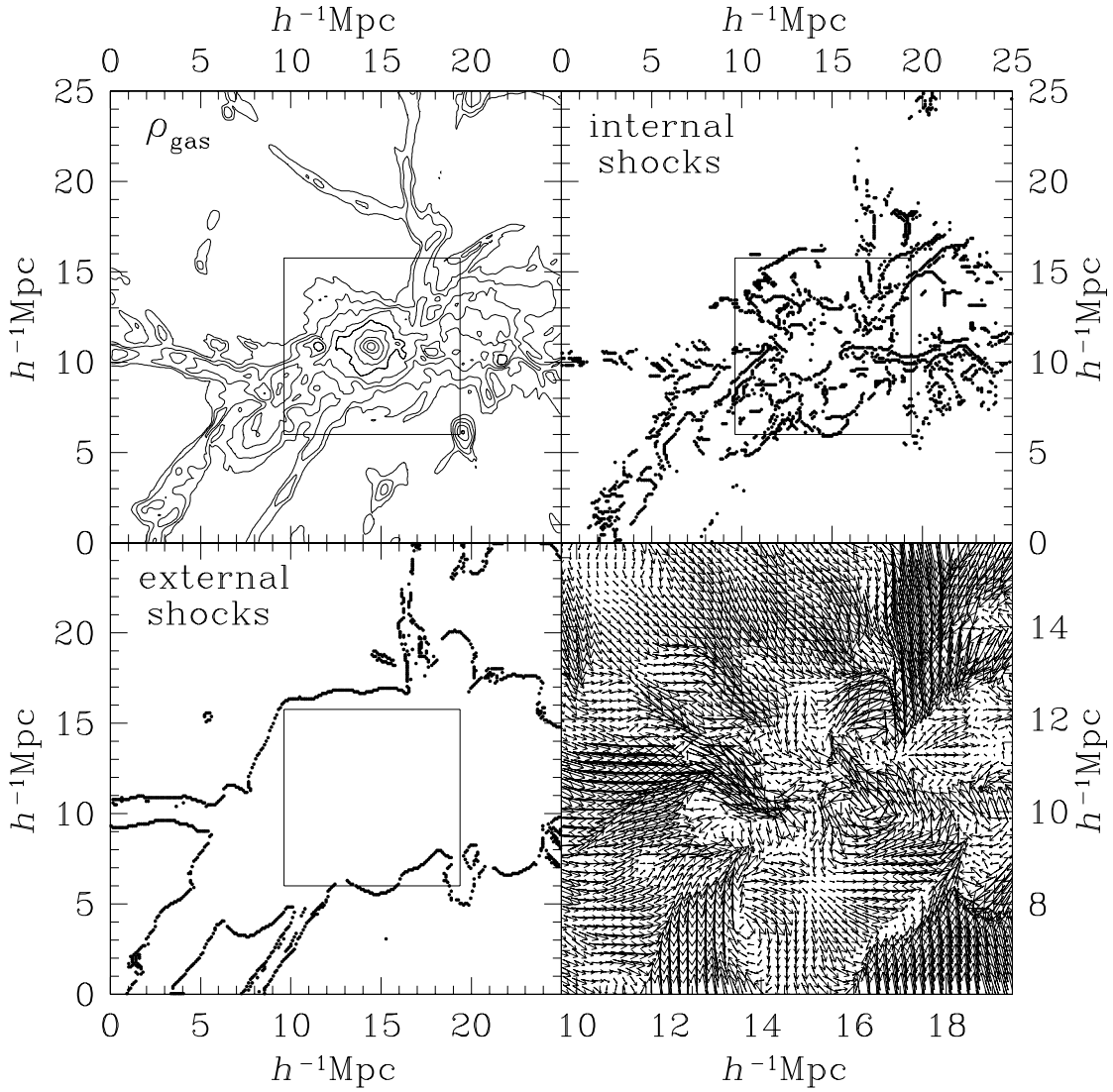

FIG. 3.—Two-dimensional slice of (25 h^{-1} Mpc)^2 around a complex including a cluster of X-ray emission-weighted temperature $T_X \approx 3.3$ at $z = 0$, showing gas density, internal and external shock distributions, and velocity field. For clarity, the velocity field is shown in a zoomed region of (12.5 h^{-1} Mpc)^2 centered at the cluster.

particular, that a spherical cluster of $T_X = 3.3$ keV has the first caustic at $R_c \approx 3.5\ h^{-1}$ Mpc from the center in our ΛCDM model (Ryu & Kang 1997), around which the external shock would be located. That is well inside the external accretion shock in this simulated cluster complex.

We will now estimate some quantitative measures of shock frequency. To start, we computed the surface area of identified shocks per logarithmic Mach number interval, $dS(M, z)/d\log M$, normalized by the volume of the simulation box. This provides an effective inverse comoving mean distance between shock surfaces. In this accounting, each shock center contributes a surface $1.19(\Delta l)^2$, which is the mean projected area within a three-dimensional zone for random shock normal orientations. The upper two panels of Figure 5 show $dS(M, z)/d\log M$ for external and internal shocks at several epochs in the simulation with 1024^3 grid zones. Table 1 lists the integrated mean shock separation, $1/S(z)$, along with the mean values of the shock Mach number, the shock speed, the preshock sound speed, and the preshock gas density.

Several important points are apparent. (1) The two populations of shocks have distinctive distributions of shock surfaces, $dS(M, z)/d\log M$, implying they are induced by flows of different characteristics. The area distribution of external shock surfaces peaks at $M \approx 3$–5, extending up to $M \sim 100$ or higher. In contrast, the comoving area of internal shocks increases to the weakest shocks we identified in our analysis (i.e., $M = 1.5$). (2) While the comoving area of external shock surfaces has not changed much since $z \lesssim 2$, that of internal shocks has increased significantly. The former behavior reflects the fact that the bounding shapes associated with external shocks have evolved toward simpler shapes to almost balance the increasing comoving volumes enclosed. On the other hand, both the volume enclosed and the complexity of internal shocks has increased so that these shocks now include more area. At the present epoch, the total area of external shock surfaces is ~2 times of that of identified internal shocks. (3) Although the mean Mach number is higher for external shocks, the mean shock speed is actually larger for internal shock. In addition, the preshock gas density is significantly higher for internal shocks. These factors

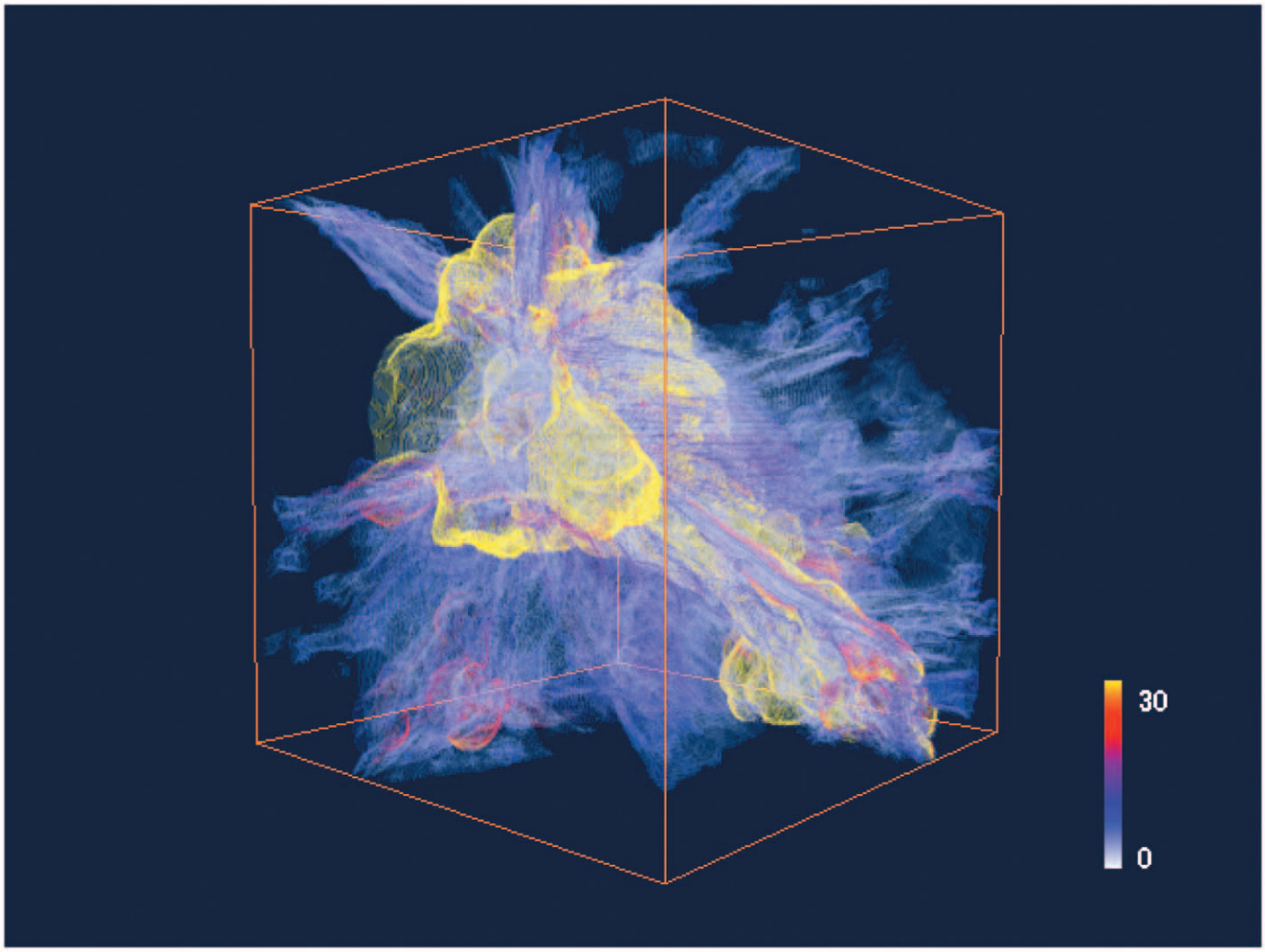

FIG. 4.—Three-dimensional shock surfaces in a volume of $(25\ h^{-1}\ \mathrm{Mpc})^3$ around the same complex as in Fig. 3. The color bar shows the values of Mach numbers of shock surfaces.

enhance their dynamical importance (see the next section). (4) We found that most clusters and groups with $T_X \gtrsim 0.1$ keV have shocks within $0.5\ h^{-1}$ Mpc from the centers at present. The area distribution of these cluster shocks, shown in the upper right panel of Figure 5, fits best to

$$\frac{dS(M,\ z)}{d\log M} \propto \exp\left(-\sqrt{\frac{M}{M_{\rm ch}}}\right), \qquad (2)$$

with $M_{\rm ch} \approx 1$ in the range of $M \lesssim 10$. Their mean Mach number is ~ 4. The cluster shocks, however, actually account for only a very small fraction of identified shock surfaces. We emphasize that the statistics for the cluster shocks would have been affected by the finite resolution, $\Delta l = 97.7\ h^{-1}$ kpc, as well as by the exclusion of physical processes such as radiative cooling and feedback from galaxies and stars that influence conditions inside cluster cores. Still, it is significant that, compared with the distribution of binary merger shocks studied

TABLE 1
MEAN FLOW QUANTITIES OF EXTERNAL/INTERNAL SHOCKS AT SEVERAL DIFFERENT EPOCHS

z	$1/S^{a}$	$S_{\rm ext}/S_{\rm int}$	$\langle M\rangle_{\rm ext}$	$\langle M\rangle_{\rm int}$	$\langle v_{\rm sh}\rangle_{\rm ext}{}^{a}$	$\langle v_{\rm sh}\rangle_{\rm int}{}^{a}$	$\langle c_s\rangle_{\rm ext}{}^{a}$	$\langle c_s\rangle_{\rm int}{}^{a}$	$\langle \rho_{\rm sh}\rangle_{\rm ext}{}^{a}$	$\langle \rho_{\rm sh}\rangle_{\rm int}{}^{a}$
0.....	4.4	2.1	8.0	3.2	123	226	15.3	82	1.05	6.78
0.2.....	4.4	2.3	8.1	3.3	123	230	15.3	83	1.12	7.15
0.5.....	4.5	2.8	8.0	3.3	122	231	15.3	83	1.25	7.86
1.....	5.0	3.7	7.5	3.4	114	214	15.3	76	1.48	8.87
1.5.....	5.7	5.0	7.0	3.4	107	196	15.3	69	1.79	10.3
2.....	6.8	6.6	6.5	3.4	100	177	15.3	62	2.14	10.9

[a] Lengths in units of $(1+z)^{-1}\ h^{-1}$ Mpc, speeds in km s^{-1}, and density compared to the mean comoving density of gas $\langle \rho_{\rm gas}\rangle(z)$, respectively.

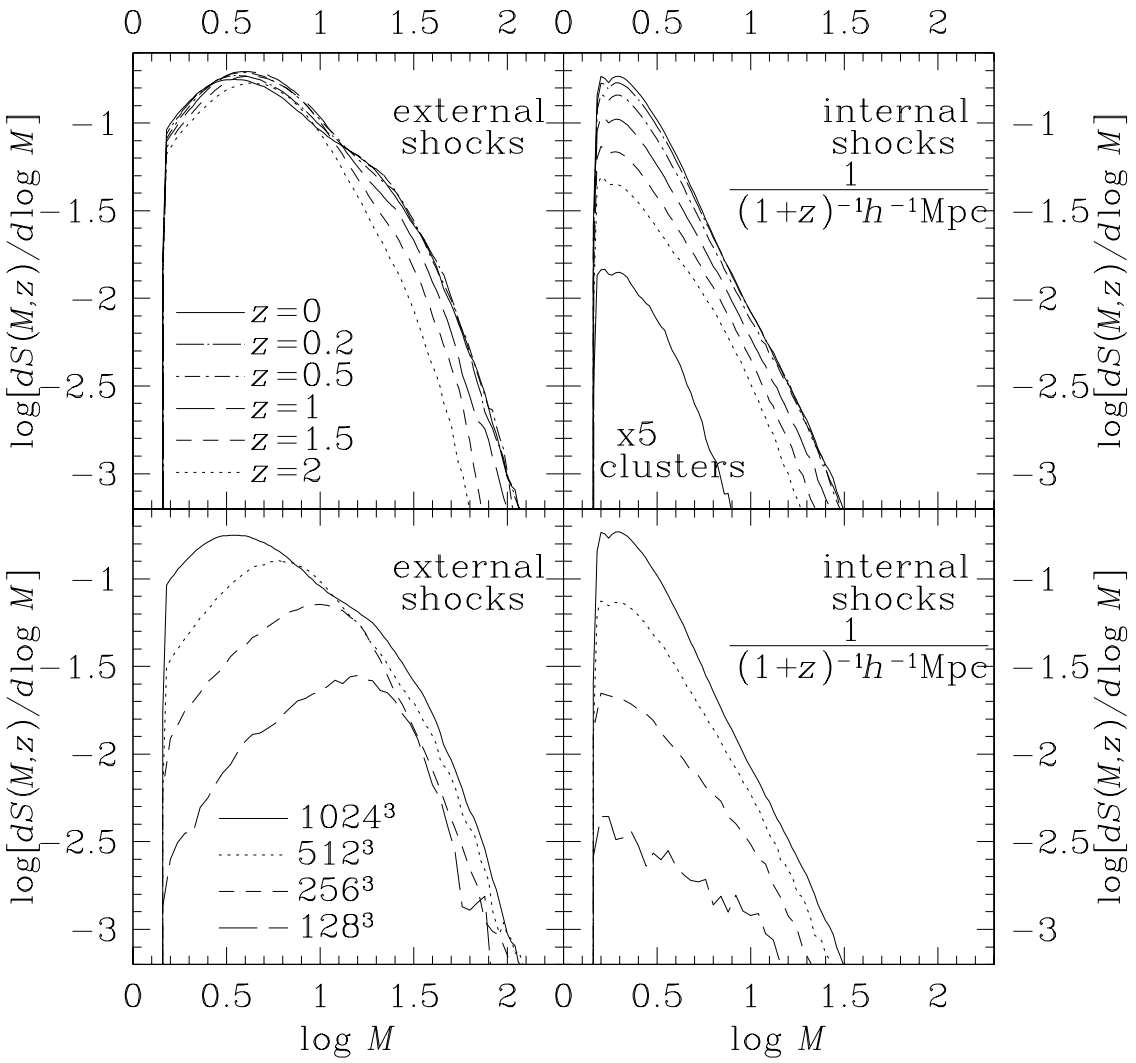

FIG. 5.—*Top panels*: Inverse of the mean comoving distance between shock surfaces with Mach number between log M and log $M + d(\log M)$ at different redshifts, $dS(M, z)$, for external shocks and internal shocks in the simulation with 1024^3 grid zones. *Curve labeled by clusters*: Quantity for shocks inside clusters and groups at present, which was multiplied with 5 for clarity (see the text for details). *Bottom panels*: Same quantity at $z = 0$ in the simulations with different resolutions of 1024^3–128^3.

in Gabici & Blasi (2003), shocks with higher Mach numbers are more common in the environments of clusters and groups in our simulation. This difference is because our cluster shock population includes accretion shocks created by infall from filaments and sheets to knots and flow shocks generated by chaotic supersonic motions, as well as those induced by hierarchical merging. Internal accretion shocks are especially strong, with a typical Mach number of several (see § 2.2).

The lower two panels of Figure 5 show $dS(M, 0)/d \log M$ for external and internal shocks at $z = 0$ in the simulations, with different numerical resolutions of 1024^3–128^3 grid zones. Table 2 lists the integrated surface area, $S(0)$, along with the mass of the gas that went through shocks at least once, $\mathcal{M}_{\rm sg}(0)$, and the total gas thermal energy inside the computational box, $\mathcal{E}_{\rm th}(0)$, at the present epoch in the simulations with 1024^3–64^3 grid zones. The shocked gas mass, $\mathcal{M}_{\rm sg}$ was estimated by summing the mass of gas with $T > 10^4$ K. We expect that finite resolution would affect the statistics of shocks in two different ways: (1) some shocks, especially weak ones with low Mach numbers, may not have been captured in the hydrodynamic part of simulations, and (2) they may not have been identified by our postprocessing shock identification scheme, especially in the regions with complex three-dimensional flow structures. The former causes quantities such as $\mathcal{M}_{\rm sg}$ and $\mathcal{E}_{\rm th}$ to be underestimated. On the other hand, the latter reduces the estimated value of $S(z)$, and hence, the estimation of shock dissipation (see the

TABLE 2
SHOCK-ASSOCIATED QUANTITIES MEASURED WITH DIFFERENT RESOLUTIONS

Resolution	$1/S^{\rm a}$	$S_{\rm ext}/S_{\rm int}$	$\mathcal{M}_{\rm sg}{}^{\rm a}$	$\mathcal{E}_{\rm th}{}^{\rm a}$
1024^3	4.4	2.1	0.73	1.42
512^3	7.3	3.2	0.69	1.30
256^3	14	5.4	0.61	1.13
128^3	39	9.6	0.45	0.87
64^3	260	28	0.19	0.40

[a] Lengths in units of h^{-1} Mpc, mass compared to total gas mass inside the computational box $\mathcal{M}_{\rm gas}$, and energy in units 10^{64} h^{-1} ergs, respectively.

next section). We see that $\mathscr{M}_{sg}$ and $\mathscr{E}_{th}$ converge rather quickly, and their converged values should be within $\sim$10% or so of those from the simulation with 1024^3. This indicates that the ability of our code to capture shocks is not the major limitation. The convergence of the mean shock separation, $1/S$ and S_{ext}/S_{int}, is not as obvious from the table. The difficulties in reaching final convergence in these quantities is evident in Figure 5. Detection of strong shocks with $M \gtrsim 10$, especially strong external shocks, is relatively robust in the simulation data with 256^3 or more grid zones. However, the area spanned by weak shocks continues to increase with resolution, reflecting the increased flow complexity captured inside nonlinear structures. The quantities of $1/S$ and S_{ext}/S_{int} are, however, also plotted in Figure 8, where it is evident that convergence is underway between the two highest resolution simulations. It is likely that $1/S \sim 4\ h^{-1}$ Mpc and $S_{ext}/S_{int} \sim 2$. It is, then, interesting to note that since the volume of the nonlinear structures where internal shocks are found is $\sim$1/10 of the entire computed volume, the mean distance between internal shock surfaces is $\sim 1\ h^{-1}$ Mpc within the nonlinear structures, which is comparable to the scale of the nonlinear structure involved. This conclusion, of course, includes the caveats that only shocks with $M \geq 1.5$ have been counted and that we have omitted from the simulations physics likely to influence shock formation inside cluster cores. Accepting the above limitations, we argue in the next section from estimations of the gas thermal energy dissipated at shocks and the mass passed through external shocks that the identification of dynamically important shocks should be complete within an error of the order of 10% in the simulation data with 1024^3 grid zones.

4. ENERGY DISSIPATION AT SHOCKS

As the first step to quantitative estimates of the gas thermal energy and CR energy from dissipation at cosmological shock waves, we defined the following fluxes of mass and energies at each shock center: (1) the gas mass flux incident on shocks, $f_{ms}(=\rho_1 v_{sh})$; (2) the incident kinetic energy flux, $f_\phi[=(1/2)\rho_1 v_{sh}^3]$; (3) the thermal energy flux generated at shocks, f_{th} (defined below); and (4) the CR energy extracted, i.e., nonthermal dissipation, at shocks, f_{CR} (defined below). Here subscripts 1 and 2 stand for preshock and postshock conditions, respectively.

We define thermal energy flux generated at shocks as

$$f_{th} = \left[e_{th,2} - e_{th,1}\left(\frac{\rho_2}{\rho_1}\right)^{\gamma}\right] u_2 \ . \tag{3}$$

We point out that the second term inside the brackets subtracts the effect of adiabatic compression occurred at a shock, not simply the thermal energy flux entering the shock, namely, $e_{th,1}u_1$. The ratio $f_{th}/f_\phi \equiv \delta(M)$ then defines the efficiency of shock thermalization, which is a function of Mach number only, and can be determined from the Rankine-Hugoniot jump conditions. The left panel of Figure 6 shows $\delta(M)$. As expected, $\delta(M)$ increases with Mach number, asymptotically approaching $\delta(M) \rightarrow 0.56$ for $M \gtrsim 10$.

We express the CR energy extraction rate as $f_{CR} = \eta(M) f_\phi$, where $\eta(M)$ measures the efficiency of diffusive shock acceleration for a given Mach number. To estimate this efficiency, we have used results of numerical simulations of the nonlinear evolution of CR modified quasi-parallel plane shocks (Kang et al. 2002; Kang & Jones 2002). The simulations utilize a plasma physics–based model for the leakage of thermal ions into the CR population, which depends on a single parameter measuring the enhancement of nonlinear scattering waves across the shock transition. That parameter is reasonably well limited by the theory and by plasma simulations (Malkov 1998), and, in the DSA simulation we used, typically limits the fraction of protons injected into the CR population at shocks to be of the order of $\sim 10^{-3}$. The CR acceleration efficiency characteristics of

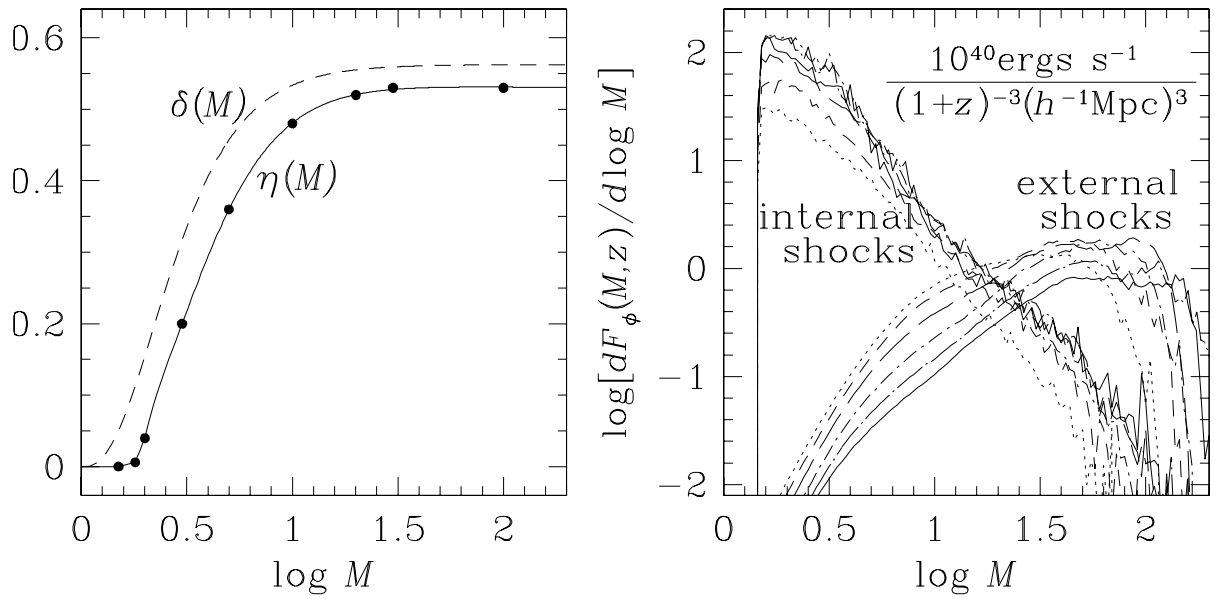

FIG. 6.—*Left panel*: Gas thermalization efficiency, $\delta(M)$, and CR acceleration efficiency, $\eta(M)$, at shocks as a function of Mach number. *Dots for* $\eta(M)$: Values estimated from numerical simulations on the basis of a DSA model and solid line is the fit. *Right panel*: Kinetic energy flux per unit comoving volume through surfaces of external and internal shocks with Mach number between $\log M$ and $\log M + d(\log M)$ at different redshifts, $dF_\phi(M, z)$, in the simulation with 1024^3 grid zones. Line types are same as those in the upper panels of Fig. 5.

our DSA model are broadly consistent with other widely used theoretical and numerical studies of nonlinear CR shocks (Malkov 1999; Berezhko et al. 1995; Ellison et al. 1996). In order to apply properties of our DSA model to cosmological shock waves, we calculated proton acceleration and accompanying CR-modified flow evolution for shocks with $v_{\rm sh} = 1500$–3000 km s^{-1} propagating into media of $T_1 = 10^4$–10^8 K, assuming Bohm-type diffusion for the CRs (for details, see Kang et al. 2002). As the shock structures evolved, we determined the ratio of the total CR energy extraction during the evolution of a shock to the kinetic energy passed through the shock according to

$$\Phi_{\rm CR}(t) \equiv \int_x E_{\rm CR}(x,\ t)dx \Big/ \left(\tfrac{1}{2}\rho_1 v_{\rm sh}^3 t\right) . \qquad (4)$$

The values of $\Phi_{\rm CR}(t)$ quickly reached approximate time-asymptotic values, after which the shock structures evolved approximately self-similarly. These asymptotic values of $\Phi_{\rm CR}(t)$ were taken as our estimates for $\eta(M)$.

The left panel of Figure 6 shows the resulting CR acceleration efficiency, $\eta(M)$, along with the gas thermalization efficiency $\delta(M)$. Both $\delta(M)$ and $\eta(M)$ increase with Mach number. In strong, high Mach-number shocks, $\eta(M)$ approaches the asymptotic value of $\eta(M) \rightarrow\sim 0.53$. We see that $\delta(M)$ is somewhat larger than $\eta(M)$ over all Mach numbers. On the other hand, we note that $\delta(M)$ was computed for purely gasdynamical shocks; that is, without accounting for energy removal into CRs and enhanced adiabatic compression within the CR shock precursor. If nonlinear dynamical feedback of CRs was included self-consistently in estimating $\delta(M)$, the resulting $\delta(M)$ would be somewhat smaller than that shown in Figure 6.

From the above gas mass and kinetic energy fluxes at each shock center, we calculated the associated fluxes through surfaces of shocks with Mach number between $\log M$ and $\log M + d(\log M)$ at different redshifts; i.e., $dF_{\rm ms}(M,\ z)$ and $dF_\phi(M,\ z)$, respectively. We also calculated the similarly defined fluxes of gas thermal and CR energies dissipated at shocks as $dF_{\rm th}(M,\ z) = dF_\phi(M,\ z) \times \delta(M)$ and $dF_{\rm CR}(M,\ z) = dF_\phi(M,\ z) \times \eta(M)$, respectively. The right panel of Figure 6 illustrates $dF_\phi(M,\ z)/d\log M$ per unit comoving volume for external and internal shocks at different redshifts in the simulation with 1024^3 grid zones. A noticeable point is that the kinetic energy flux and also the gas mass flux through external shocks were larger in the past. This is because the preshock gas density was larger in the past. However, the kinetic energy flux through internal shocks has been more or less constant since $z \sim 1.5$ and was smaller before that.

To provide measures of the roles of shocks over time, we integrated from $z = 2$ to $z = 0$ the gas mass and kinetic energy that passed through shock surfaces, and the gas thermal and CR energies dissipated at shock surfaces as

$$\frac{dY_i(M)}{d\log M} = \frac{1}{\mathcal{N}_i}\int_{z=2}^{z=0} \frac{dF_i(M,\ z)}{d\log M} dt , \qquad (5)$$

where the subscript $i \equiv$ ms , ϕ, th, and CR stands for the four fluxes defined above. The quantities were normalized to either the shocked gas mass, $\mathcal{N}_{\rm ms} \equiv \mathcal{M}_{\rm sg}(z=0)$, for mass, or to the total gas thermal energy inside the computational box, $\mathcal{N}_i \equiv \mathcal{E}_{\rm th}(z=0)$, for energies (see Table 2). We also summed these time-integrated measures to calculate the associated global shock-processed quantities,

$$Y_i(>M) = \int_\infty^M \left[\frac{dY_i(M)}{d\log M}\right] d\log M . \qquad (6)$$

The quantities $Y_{\rm ms}$ and $dY_{\rm ms}(M)/d\log M$ not only measure the total mass that passed through shocks in the $z = 2$ to $z = 0$ interval, but also, by way of their normalization, measure the mean number of times that gas has been subjected to shock dissipation. Meanwhile, Y_ϕ and its derivative measure the total kinetic energy that has been subject to shock dissipation. On the other hand, $Y_{\rm th}$ and $Y_{\rm CR}$ compare the total thermal and CR energies that have resulted from shock dissipation.

Figure 7 shows $dY_i(M)/d\log M$ and $Y_i(>M)$ for external and internal shocks in the simulation with 1024^3 grid zones. Again, several important points are apparent. (1) The plots for $dY_{\rm ms}(M)/d\log M$ and $Y_{\rm ms}(>M)$ indicate that more mass has passed through internal shocks than external shocks. With $Y_{\rm ms}(\geq 1.5) \approx 2.2$ for internal shocks, the mass inside the nonlinear structures of sheets, filaments, and knots has been shocked, on average, twice or so by internal shocks from $z = 2$ to 0. But we note that $dY_{\rm ms}(M)/d\log M$ for internal shocks increases to $M = 1.5$, the lowest Mach number we kept, and weak shock identification is not fully converged yet with this numerical resolution. So the above value of 2.2 should be regarded as the lower limit. (2) On the other hand, since gas enters the nonlinear structures by passing through external shocks, $Y_{\rm ms}(\geq 1.5)$ for external shocks (i.e., the mass passed through external shocks from $z = 2$ to 0) should match the increase in the shocked gas mass, $\mathcal{M}_{\rm sg}$, from $z = 2$ to 0. In the simulation with 1024^3 grid zones, we get $Y_{\rm ms}(\geq 1.5) = 0.35$ for external shocks, while $0.42 = (0.73$–$0.42)/0.73$ is expected with $\mathcal{M}_{\rm sg}(z=2) = 0.42\mathcal{M}_{\rm gas}$ and $\mathcal{M}_{\rm sg}(z=0) = 0.73\mathcal{M}_{\rm gas}$ (where $\mathcal{M}_{\rm gas}$ is the total gas mass in the computational box). Although a fraction of the hot gas may have been heated above 10^4 K by adiabatic compression in void regions or by weak shocks with $M < 1.5$, some of this discrepancy could be due to the undercounting of external shocks. So we estimate an error of $\sim$10% or so in the completeness of the identification of external shocks. (3) The lower two panels of Figure 7 show that internal shocks play a more important role than external shocks in the dissipating energy associated with structure formation. Specifically, internal shocks with $2 \lesssim M \lesssim 4$ account for about one-half of the dissipation. While the thermal energy generation peaks for shocks in the range $2 \lesssim M \lesssim 3$, the CR energy extraction peaks in the range $3 \lesssim M \lesssim 4$. Miniati (2002) identified shocks with $4 \lesssim M \lesssim 5$ as the most important in gas thermalization. Our result indicates a somewhat lower Mach number range, because we found more weaker shocks in our simulation data. This difference is probably due to our greater resolution (see Fig. 5), as well as improved shock capturing in the present code and a more sophisticated shock identification scheme. (4) The amount of thermal energy generated at shocks from $z = 2$ to 0 was computed to be $\sim$1.5 times the current gas thermal energy in the simulation with 1024^3 grid zones. Since no other heating or cooling physics was included, there are two likely contributors to the difference. First, we attribute some of the difference to adiabatic expansion of nonlinear structures after formation. Expansion of $\sim$8.5% along each dimension would be enough to reduce the gas thermal energy by a factor of 1.5.

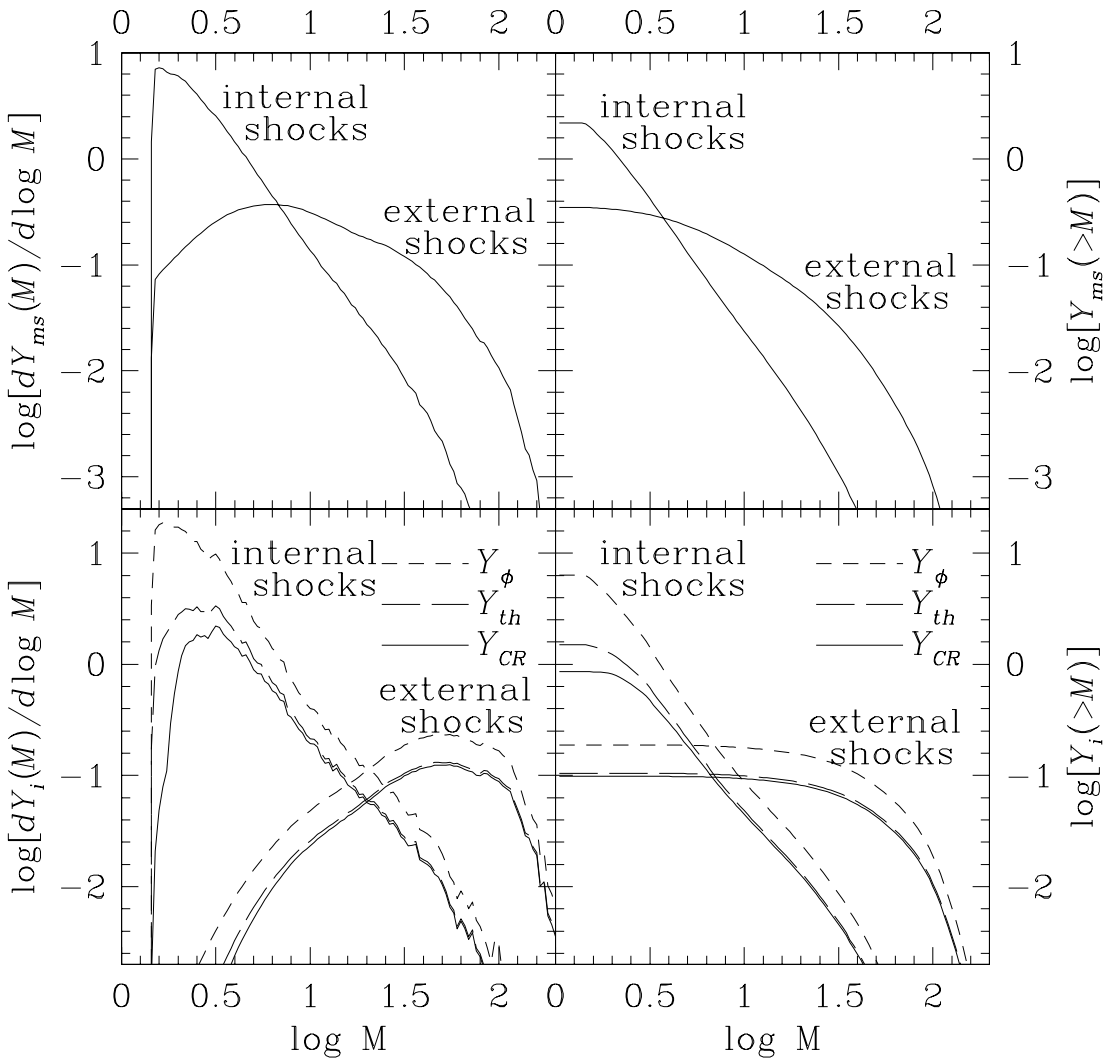

FIG. 7.—*Upper left panel*: Mass, $dY_{\rm ms}(M)$, processed through surfaces of external and internal shocks with Mach number between $\log M$ and $\log M + d(\log M)$, from $z = 2$ to $z = 0$. *Upper right panel*: Mass, $Y_{\rm mass}(> M)$, processed through surfaces of external and internal shocks with Mach number greater than M, from $z = 2$ to $z = 0$. *Lower left panel*: Kinetic energy, $dY_\phi(M)$, thermal energy, $dY_{\rm th}(M)$, and CR energy, $dY_{\rm CR}(M)$, processed through surfaces of external and internal shocks with Mach number between $\log M$ and $\log M + d(\log M)$, from $z = 2$ to $z = 0$. *Lower right panel*: Same energies, $Y_\phi(> M)$, $Y_{\rm th}(> M)$, $Y_{\rm CR}(> M)$, processed through surfaces of external and internal shocks with Mach number greater than M, from $z = 2$ to $z = 0$. The mass and energies are normalized to the shocked gas mass, $\mathscr{M}_{\rm sg}$, and the total gas thermal energy, $\mathscr{E}_{\rm th}$, inside simulation box at $z = 0$, respectively. All plots are from the simulation data with 1024^3 grid zones.

In addition, some of the discrepancy could be the result of multiple counting of internal shocks in the regions with complex flow structures. So again, we put an error of a few 10%, at most, in the completeness of the identification of shocks. (5) With the DSA model we adopted (Kang et al. 2002; Kang & Jones 2002), the ratio of the CR to gas thermal energies dissipated at cosmological shock waves with the Mach number greater than 1.5 is $Y_{\rm CR}(\geq 1.5)/Y_{\rm th}(\geq 1.5) \approx 1/2$. (6) There are many shocks with $M \lesssim 2$, but they are not important in energetics. Hence, although we ignored the shocks with $M < 1.5$ in this work, that should not significantly impact quantitative energetics results presented here.

Figure 8 shows $Y_i(\geq 1.5)$ through all shock surfaces in the simulations with different resolution of 1024^3–64^3 grid zones. Note that Y_i's were normalized with $\mathscr{M}_{\rm sg}$ and $\mathscr{E}_{\rm sg}$ for a given resolution (Table 2). Yet, for instance, Y_ϕ, the integrated kinetic energy flux through shock surfaces, decreases in the plot by 60% from 1024^3 to 512^3 and by 95% from 512^3 to 256^3. On the other hand, $\mathscr{E}_{\rm sg}$, the total gas thermal energy inside the computational box, decreases only by 8% from 1024^3 to 512^3 and 13% from 512^3 to 256^3. This reinforces the statements in the previous section that the error in quantitative assessments of this paper comes mostly from shock identification in the postprocessing analysis rather than shock capturing in the code. This also shows that our estimation of an error of the order of 10% in the data of the 1024^3 simulation is consistent with resolution convergence.

5. SUMMARY

We identified and studied shock waves with Mach number $M \geq 1.5$ in a set of cosmological N-body/hydrodynamic simulations for a ΛCDM universe in a cubic box of comoving size $100\,h^{-1}$ Mpc. To facilitate the analysis of their properties, the cosmological shock waves were classified as external and internal shocks, depending on whether or not the preshock gas was previously shocked. External

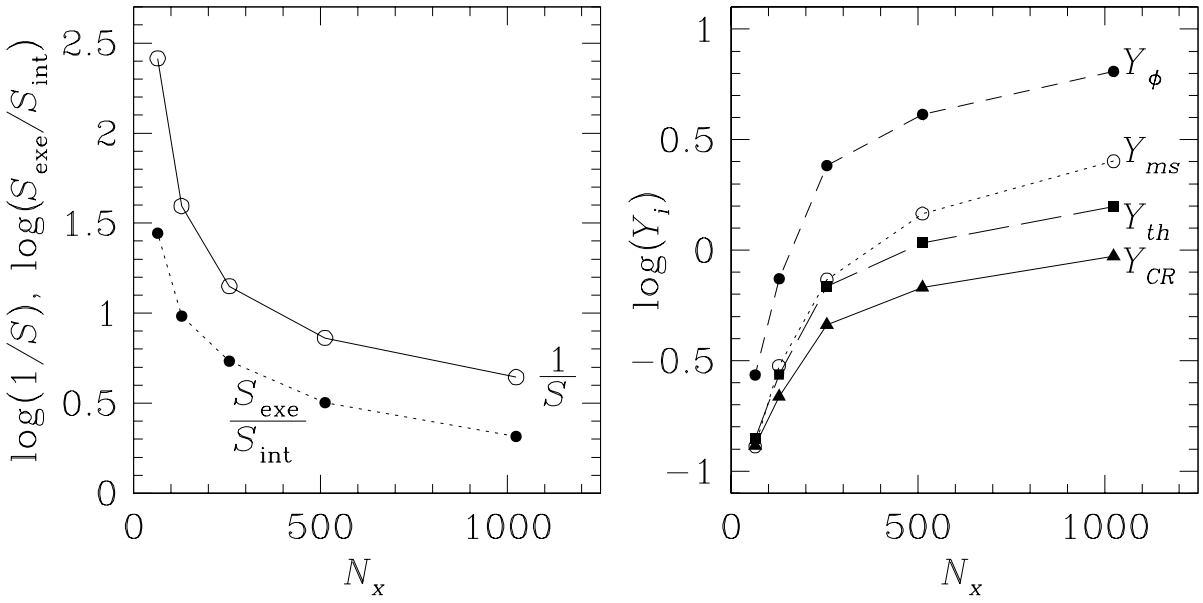

FIG. 8.—*Left panel*: Mean shock separation at $z = 0$, $1/S$, and its ratio for two shock populations, $S_{\rm ext}/S_{\rm int}$, for identified shocks with $M \geq 1.5$ in the simulations of different resolutions with number of grid points along one-dimension, $N_{\rm X} = 64$, 128, 256, 512, and 1024. *Right panel*: Integrated mass, $Y_{\rm ms}$, and energies, Y_ϕ, $Y_{\rm th}$, $Y_{\rm CR}$, processed through all identified shocks with $M \geq 1.5$ in the simulations of different resolutions. The mass and energies are normalized to the shocked gas mass, $\mathcal{M}_{\rm sg}$, and the total gas thermal energy, $\mathcal{E}_{\rm th}$, of given resolution, inside simulation box at $z = 0$, respectively.

shocks form around outermost surfaces that encompass nonlinear structures so they are, by nature, accretion shocks that decelerate the previously unshocked intergalactic gas infalling toward sheets, filaments, and knots. Internal shocks are produced within those nonlinear structures by accretion flows of previously shocked gas from sheets to filaments and knots and from filaments to knots, by merging of subclumps, or by chaotic flow motions induced in the course of hierarchical clustering.

For all shocks of $M \geq 1.5$ identified in the simulation of highest resolution, the mean distance between shock surfaces, the inverse indicator of shock occurrence, is $\sim 4\ h^{-1}$ Mpc at present. Further, external shocks are more extensive, with their surface area ~ 2 times larger than that of identified internal shocks. With the volume of nonlinear structures, which is $\sim 1/10$ of the total volume, the mean distance between internal shock surfaces is $\sim 1\ h^{-1}$ Mpc within nonlinear structures. Although external shocks typically have higher Mach numbers, internal shocks have higher shock speed and higher preshock gas density. As a result, internal shocks are responsible for $\sim 95\%$ of gas thermalization and for $\sim 90\%$ of CR acceleration at shocks, and they process about 6 times more gas mass through shock surfaces than external shocks do from $z = 2$ to $z = 0$. Internal shocks with $2 \lesssim M \lesssim 4$ are especially important in energy dissipation, contributing about one-half of the total. By adopting a model of CR proton acceleration based on nonlinear diffusive shock simulations (Kang et al. 2002), our study predicts that the ratio of the CR to gas thermal energies dissipated at all cosmological shocks through the history of the universe could be about one-half. Due to long CR proton trapping times and energy-loss lifetimes, they should fill the volumes inside filaments and sheets as well as in clusters and groups. Short electron lifetimes, however, lead that population to depend on other factors (Miniati et al. 2001a). The existence of substantial CR populations could have affected the evolution and the dynamical status of the large-scale structure of the universe (Ensslin et al. 1997).

The examination of results from simulations of different resolutions showed that the convergence with resolution in shock identification is slower than in shock capture within the simulation itself. Consistency checks and resolution convergence analysis lead to error estimates of the order of 10% in our quantitative estimates of the accounting of and energy dissipation in cosmological shock waves.

Strong external shocks are energetically less important than moderate-strength internal shocks. However, it is important to keep in mind that the large curvature radii and long lifetimes of these shocks make them viable candidates to accelerate CRs to ultra high energies of several 10^{19} eV (Norman, Melrose, & Achterberg 1995; Kang, Ryu, & Jones 1996).

The Mach number distribution and the amount of energy dissipation at cosmological shocks have significant implications for several cosmological observations, such as radio and γ-ray emissions, as well as X-ray emission from the ICM and contribution to the cosmic γ-ray background from CRs accelerated at these shocks (Loeb & Waxmann 2000; Miniati et al. 2001a, 2001b; Miniati 2002). These important issues, along with the observational manifestation of cosmological shock waves, will be considered in future studies.

D. R. and H. K. were supported by KOSEF through Astrophysical Research Center for the Structure and Evolution of Cosmos (ARCSEC). E. H. and T. W. J. were supported by the NSF (AST 00-71167), NASA (NAG5-10774), and the University of Minnesota Supercomputing Institute. Numerical simulations utilized the Grand Challenge Program of the KISTI Supercomputing Center. We thank Peter L. Biermann and an anonymous referee for constructive comments on the manuscript.

REFERENCES

Bennett, C. L., et al. 2003, ApJ, in press
Berezhko, E. G., Ksenofontov, L. T., & Yelshin, V. K. 1995, Nucl. Phys. B, 39A, 171
Blandford, R. D., & Eichler, D. 1987, Phys. Rep., 154, 1
Cen, R., & Ostriker, J. P. 1999, ApJ, 514, 1
Colafrancesco, S., & Blasi, P. 1998, Astropart. Phys., 9, 227
Davé, R., et al. 2001, ApJ, 552, 473
Ellison, D. C., Baring, M. G., & Jones, F. C. 1996, ApJ, 473, 1029
Ensslin, T. A., Biermann, P. L., Kronberg, P., & Wu, X.-P. 1997, ApJ, 447, 560
Feretti, L. 2003, in ASP Conf. Ser. 301, Matter and Energy in Clusters of Galaxies, ed. S. Bowyer & C.-Y. Hwang (San Francisco: ASP), in press
Fusco-Femiano, R., Dal Fiume, D., Feretti, L., Giovannini, G., Grandi, P., Matt, G., Molendi, S., & Santangelo, A. 1999, ApJ, 513, L21
Gabici, S., & Blasi, P. 2003, ApJ, 583, 695
Giovannini, G., & Feretti, L. 2000, NewA, 5, 335
Haiman , Z., & Holder, G. P. 2003, ApJ, submitted (astro-ph/0302403)
Kang, H., & Jones, T. W. 2002, J. Korean Astron. Soc., 35, 159
Kang, H., Jones, T. W., & Gieseler, U. D. J. 2002, ApJ, 579, 337
Kang, H., Ryu, D., & Jones, T. W. 1996, ApJ, 456, 422
Kennel, C. F., Edmiston, J. P., & Hada, T. 1985, in Collisionless Shocks in the Heliosphere (AGU Monogr. 34; Washington: AGU), 1
LeVeque, R. J. 1997, in 27th Saas-Fee Advanced Course Lecture Notes, Computational Methods in Astrophysical Fluid Flows, ed. O. Steiner & A. Gautschy (Berlin: Springer), 1
Lieu, R., Ip, W.-H., Axford, I. W., & Bonamente, M. 1999, ApJ, 510, L25
Lieu, R., Mittaz, J. P. D., Bowyer, S., Lockman, F. J., Hwang, C.-Y., & Schmitt, J. H. M. M. 1996, ApJ, 458, L5
Loeb, A., & Waxmann, E. 2000, Nature, 405, 156
Malkov, M. A. 1998, Phys. Rev. E, 58, 4911
———. 1999, ApJ, 511, L53
Malkov M. A., & Drury, L. O. 2001, Rep. Prog. Phys., 64, 429
Miniati, F. 2002, MNRAS, 337, 199
Miniati, F., Jones, T. W., Kang, H., & Ryu. D. 2001a, ApJ, 562, 233
Miniati, F., Ryu, D., Kang, H., & Jones, T. W. 2001b, ApJ, 559, 59
Miniati, F., Ryu, D., Kang, H., Jones, T. W., Cen, R., & Ostriker, J. 2000, ApJ, 542, 608
Norman, C. A., Melrose, D. B., & Achterberg, A. 1995, ApJ, 454, 60
Quest, K. B. 1988, in Proc. 6th Intl. Solar Wind Conf., ed. V. J. Pizzo (Boulder: NCAR), 503
Quilis, V., Ibanez, J. M. A., & Saez, D. 1998, ApJ, 502, 518
Reimer, O., Pohl, M., Sreekumar, P., & Mattox, J. R. 2003, ApJ, 588, 155
Ryu, D., & Kang, H. 1997, MNRAS, 284, 416
Ryu, D., Ostriker, J. P., Kang, H., & Cen, R. 1993, ApJ, 414, 1
Scharf, C. A., & Mukherjee, R. 2002, ApJ, 580, 154
Wentzel, D. G. 1974, ARA&A, 12, 71